Bulletin of Earthquake Engineering

Validation of regional physics-based ground motion scenarios: the case of the Mw 4.9 2019 Le Teil earthquake in France

--Manuscript Draft--

Manuscript Number:	
Full Title:	Validation of regional physics-based ground motion scenarios: the case of the Mw 4.9 2019 Le Teil earthquake in France
Article Type:	Original Article
Keywords:	physics-based numerical simulation; seismic wave propagation; seismic site effects; seismic safety; benchmark; nuclear power plant
Corresponding Author:	Chiara Smerzini Politecnico di Milano Milano, Milano ITALY
Corresponding Author Secondary Information:	
Corresponding Author's Institution:	Politecnico di Milano
Corresponding Author's Secondary Institution:	
First Author:	Chiara Smerzini
First Author Secondary Information:	
Order of Authors:	Chiara Smerzini
	Manuela Vanini
	Roberto Paolucci
	Philippe Renault
	Paola Traversa
Order of Authors Secondary Information:	
Funding Information:	swissnuclear — Prof. Roberto Paolucci
Abstract:	In this paper, a comprehensive validation exercise of 3D physics-based numerical simulations (PBS) of seismic wave propagation is presented for a low-to-moderate seismicity area in the south east of France, within the Rhône River Valley, that hosts several operating nuclear installations. This area was hit on Nov 11, 2019, by an unusually damaging Mw 4.9 earthquake (Le Teil event). The numerical code SPEED (http://speed.mox.polimi.it/), developed at Politecnico di Milano, Italy, was used to validate the simulations against the available recordings. When comparing simulations with records, a good to excellent agreement was found up to 8-10 Hz, showing that, even without a very detailed 3D numerical model of the medium, the PBS may provide realistic broadband predictions of earthquake ground motion. This also demonstrates that PBS, if suitably calibrated and validated, may be either an alternative or a useful complement to empirical ground motion models. Referring to the seismic risk evaluation of strategic and critical structures, infrastructures and industrial plants, such as nuclear power plants, the failure of which during an earthquake may endanger safety of population and cause environmental disasters, the 3D PBS may throw light on region- and site-specific features of ground shaking, especially in near-source conditions, that are typically poorly constrained in empirical models.
Suggested Reviewers:	Gabriele Ameri gabriele.ameri@seister.fr expert in seismic hazard analysis and ground motion, with focus on French context
	Fabrice Cotton fabrice.cotton@gfz-potsdam.de

	expert in ground-motion models with focus on low seismicity areas
	Stefano Parolai sparolai@inogs.it expert in seismology
	Cécile Cornou cecile.cornou@univ-grenoble-alpes.fr expert in seismic hazard with focus on site effects
	Floriana Petrone florianapetrone@unr.edu expert in engineering applications of physics-based numerical simulations

Validation of regional physics-based ground motion scenarios: the case of the Mw 4.9 2019 Le Teil earthquake in France

By C. Smerzini, M. Vanini, R. Paolucci, P. Renault, P. Traversa

---

Abstract

In this paper, a comprehensive validation exercise of 3D physics-based numerical simulations (PBS) of seismic wave propagation is presented for a low-to-moderate seismicity area in the south east of France, within the Rhône River Valley, that hosts several operating nuclear installations. This area was hit on Nov 11, 2019, by an unusually damaging Mw 4.9 earthquake (Le Teil event). The numerical code SPEED (http://speed.mox.polimi.it/), developed at Politecnico di Milano, Italy, was used to validate the simulations against the available recordings. When comparing simulations with records, a good to excellent agreement was found up to 8-10 Hz, showing that, even without a very detailed 3D numerical model of the medium, the PBS may provide realistic broadband predictions of earthquake ground motion. This also demonstrates that PBS, if suitably calibrated and validated, may be either an alternative or a useful complement to empirical ground motion models. Referring to the seismic risk evaluation of strategic and critical structures, infrastructures and industrial plants, such as nuclear power plants, the failure of which during an earthquake may endanger safety of population and cause environmental disasters, the 3D PBS may throw light on region- and site-specific features of ground shaking, especially in near-source conditions, that are typically poorly constrained in empirical models.

Keywords: physics-based numerical simulation; seismic wave propagation; seismic site effects; seismic safety; benchmark; nuclear power plant.

---

1 Introduction

The recent history of nuclear power plants (NPP) affected by seismic events, such as those occurred in Japan at Kashiwazaki-Kariwa (during the July 16, 2007, Chuetsu earthquake, Mw6.6) and Fukushima (during the March 11, 2011, Tohoku earthquake, Mw9), has raised the public attention that seismic hazard may be a relevant contributor to the overall risk of NPPs.

According to IAEA safety standards (IAEA-SSG9, 2022) both empirical and direct simulation methods can be used to estimate vibratory ground motions, within either probabilistic or deterministic seismic hazard assessment. Empirical ground motion models (GMMs) represent the standard approach for ground motion characterization in a probabilistic framework, suited to account for different sources of aleatory and epistemic uncertainties, but they are also used as a standard for deterministic seismic hazard assessment. However, because of their ergodic nature, classical GMMs do not provide quantitative estimates of the region- and site-specific features of earthquake ground motion, unless empirical non-ergodic adjustments are considered (e.g., Biro and Renault, 2012; Ameri et al. 2017) or fully non-ergodic models are implemented in the considered region (e.g. Landwehr et al., 2016; Sung et al., 2022).

As an alternative approach to GMMs, 3D physics-based numerical simulations (PBS) of seismic wave propagation account for the seismic source, the propagation path and the amplification effects related to the site-specific shallow geology (e.g., Paolucci et al., 2018; McCallen et al., 2021). They are becoming more and more appealing as the performance of computer codes is growing exponentially and their use is particularly appropriate in case of complex geological configurations, coupled with near-source conditions, cases that are poorly constrained in GMMs due to small amount of recordings. Quoting IAEA-SSG9, the PBS procedures "*might be especially effective in cases where nearby faults contribute significantly to the vibratory ground motion hazard at the site and/or where the existing empirical data are limited (e.g. on the hanging wall of a nearby fault)*".

Validation of 3D PBS against recorded weak or strong ground motions is one of the key propaedeutic activities to ensure that the different input elements of PBS, namely, the seismic source and the 3D velocity model, are suitable to reproduce the recorded motions, at least up to a prescribed frequency limit.

In the framework of the SIGMA-2 Project (https://www.sigma-2.net/), funded by different industrial partners that operate in the nuclear energy sector, a benchmark on different simulation approaches for earthquake ground motion prediction was organized, with reference to the

November 11, 2019 Mw 4.9 Le Teil earthquake (El Haber et al. 2022). This earthquake occurred in a densely populated low-to-moderate seismicity region of South-Eastern France, close to the city of Montélimar within the lower Rhône Valley, at relatively short distance from two NPPs, i.e., Cruas (at an epicentral distance R_{epi} of 15 km) and Tricastin (R_{epi}=24 km). The primary goal of the benchmark was to validate and explore the potential of different ground motion simulation techniques in predicting ground motion in a low-to-moderate seismicity area, where the description of the seismic wave propagation medium is limited, the fault geometry and activity are poorly known and the earthquake records are rare.

In this paper, the simulations are carried out using the spectral element code SPEED (Mazzieri et al., 2013), which has been extensively used in the recent past to perform PBS validated on different real earthquakes (Paolucci et al., 2015; Evangelista et al., 2017; Infantino et al., 2020; Sangaraju et al., 2021) and to construct a prototype of a near-source simulated accelerograms dataset with the aim of complementing recordings datasets, still relatively sparse in such near-source conditions (Paolucci et al., 2021).

After a brief overview of the case study in Section 2, the 3D numerical model is introduced in Section 3, while the verification and numerical convergence tests are discussed in Section 4. In Section 5, simulated ground motion is successfully compared with the recorded one on a broad frequency range, up to about 8 Hz, where the convergence tests have shown that the accuracy of numerical wave propagation is reasonably preserved. Furthermore, Goodness of Fit tests show good to excellent scores. Since the main role of 3D PBS is to highlight region- and site-specific features of earthquake ground motion that cannot be resolved by the ergodic empirical GMMs, and that may lead to biased estimates for seismic hazard assessment, in Section 6 the main findings related to the 3D site amplification features in the Rhône Valley are summarized and compared with 1D approaches for site amplification estimation.

2 Case study: the Le Teil Mw 4.9 earthquake

On November 11, 2019 a seismic event of moment magnitude Mw 4.9, referred to as Le Teil earthquake, occurred in South-Eastern France, close to the city of Montélimar with about 40,000 inhabitants, within the lower Rhône Valley (see Figure 1). The earthquake hit a densely populated industrial region characterized by low-to-moderate seismic activity which hosts several operating NPPs. As previously mentioned, two nuclear facilities, namely Cruas and Tricastin, are located close to the epicenteral area of the earthquake, at about 15 km North-East and 24 km South-East of the epicenter, respectively. In spite of the moderate magnitude, the shock caused different degree of damages to approximately 900 residential buildings and several public buildings in the municipality of Le Teil, located at 4 km from the epicenter, going from light cracks in the walls to total collapse. About 200 of these housings were declared at risk of collapse. The maximum macroseismic intensity degree (EMS98 scale, Grünthal et al., 1998) I_{max}=VII-VIII was estimated for Le Teil municipality (Schlupp et al. 2021; Sira et al. 2020). The economic losses induced by the Le Teil earthquake have been estimated at around 200 MEUR for private property and at around 12 MEUR for communal properties (AFPS, 2021).

The region is characterized by a low-to-moderate seismicity, with instrumental earthquakes of maximum magnitude ranging between 3 and 4 (see orange circles in Figure 1, from SI-HEX (Cara et al., 2015) updated catalogue, https://www.franceseisme.fr/). The most significant historical earthquakes in the region (as indicated by purple dots in Figure 1) occurred south of Le Teil in 1773, 1873 the 1923, with maximum macroseismic intensities up to I_{max}=VII MSK (SISFRANCE database, www.sisfrance.net). The August 8, 1873 earthquake, at around 8 km southward from Le Teil, was the largest shock ever felt in this region, with an estimated Mw of around 4.1 and a focal depth of about 3 km (FCAT catalogue, Manchuel et al., 2018). An earthquake was located near Le Teil in November 1923, with an inferred Mw of around 3 and I_{max}=IV MSK.

From a seismotectonic point of view, the epicenter of the Le Teil earthquake is located at the boundary between the Massif Central crystalline basement and the sedimentary basin of South-Eastern France bordering the Alps mountain range. The tectonic evolution of this region was marked by several deformation phases since 200 million years (Ma), which have produced a complex structural pattern in a compressional stress regime with around 100-km-long system of faults (i.e., the Cevennes Fault System – CFS) striking NE-SW and dipping to the southeast (Delouis et al., 2019; Ritz et al. 2020).

The earthquake was generated by the seismic rupture of a segment of the La Rouvière fault (LRF, see red line in Figure 1), which is located at the North-Eastern part of the CFS. The LRF was not identified as a potentially active fault in the Database of Potentially Active Faults for Metropolitan France – BDFA (https://bdfa.irsn.fr/, Jomard et al., 2017), but it was already listed on the geological map of the Aubenas area (Elmi et al. 1996). The 8 km-long La Rouvière fault is oriented NE-SW (azimuth from N030 to N050), it dips steeply to South-East and is located between, and parallel to, the Saint Remèze fault (part of the Cévennes fault) to the North-West and the Marsanne fault to the South-East. The latter two, contrarily to the LFR, were identified as potentially active faults in the BDFA.

Geodetic, seismological and field data indicate a rupture area of about 4 km × 1.5 km, characterized by a reverse focal mechanism, with a hypocenter (44.521°N; 4.669°E) located at solely 1 km depth from the ground surface (Cornou et al. 2021; Causse et al. 2021). Ritz et al. (2020) show evidence of surface fault rupture with a permanent uplift up to 15 cm on the fault hanging wall, which is rather uncommon considering the magnitude and for this region. Such a shallow focal depth is unusual for an earthquake of tectonic origin and it is typically associated with earthquakes of anthropogenic nature, such as gas extraction induced events. Based on both in-field observations and numerical simulations, Causse et al. (2021) showed that, although the average source properties of the Le Teil earthquake (stress drop, slip distribution and rupture velocity) were consistent with common deeper earthquakes, the unusually shallow rupture produced exceptional levels of ground shaking in the immediate vicinity of the causative fault. Azimuthal and frequency dependencies of ground motion decay with distance are the object of current research works. The shallow hypocenter, together with the presence of a large limestone quarry located on the hanging wall of the LRF, motivated studies on the causal relationship between the extraction activities and the triggering of the Le Teil earthquake (De Novellis et al. 2020).

Recordings of the Le Teil event and aftershocks are available from the stations of the RESIF network (Réseau Sismologique et géodésique Français – RESIF http://seismology.resif.fr/, 1995) and of the closest stations of the EDF (Electricité de France, the French NPP operator) network. As shown by the blue triangles of Figure 1, only four stations fall within the area covered by the 3D numerical model (details of these stations are given in Table 1). These stations are the reference with respect to which the simulation results will be tested and validated. Due to the limited number of records at short epicentral distance, PBS can be effectively employed to gain insights into the main features of seismic shaking in the region.

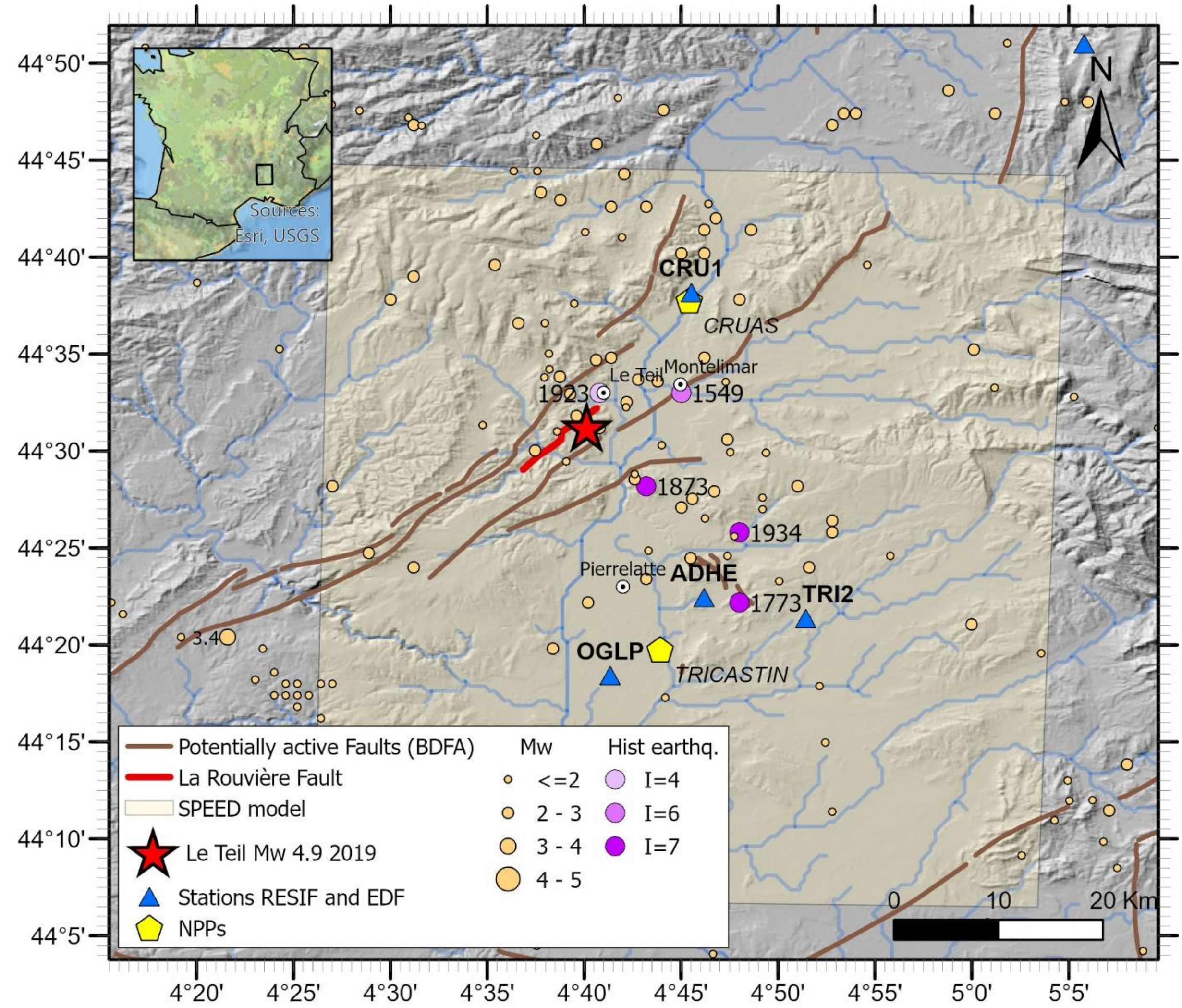

Figure 1. Seismotectonic map of the region hit by the November 11, 2019 Mw 4.9 Le Teil earthquake. The orange and purple circles are instrumental and historical earthquakes, respectively; the yellow hexagons denote the Nuclear Power Plants (NPP) in the region. The brown lines are potentially active faults mapped in the BDFA catalogue (https://bdfa.irsn.fr/), while the La Rouvière Fault (LRF), activated by the Le Teil earthquake, is in red. Blue triangles are the stations of the RESIF and EDF networks.

Table 1. Reference accelerometric stations of the RESIF network (for OGLP and ADHE) and for the EDF network (for CRU1 and TRI2 stations). The station coordinates (in WGS84) are given, with their epicentral distance (R_{epi}) from the Le Teil earthquake and the V_{S30} of the site.

Station	Lat (°N)	Lon (°E)	Elevation [m]	R_{epi} [km]	V_{S30} [m/s]
ADHE	44.374	4.770	90	18	2000
CRU1	44.636	4.759	77	15	662
OGLP	44.307	4.689	46	24	490
TRI2	44.356	4.857	141.2	24	-

3 3D numerical model of the Montélimar region

Figure 2 Figure 2shows the area modelled in this work, with the causative fault and epicenter of the Le Teil earthquake and the details of the basin shape adopted in the numerical model. The figure shows also the position of the stations used in the analyses, as well as of the Cruas and Tricastin NPPs. A geological cross-section (orthogonal to the fault rupture area, see dashed line in Figure 2) modified from Causse et al. (2021) is shown in the top right corner.

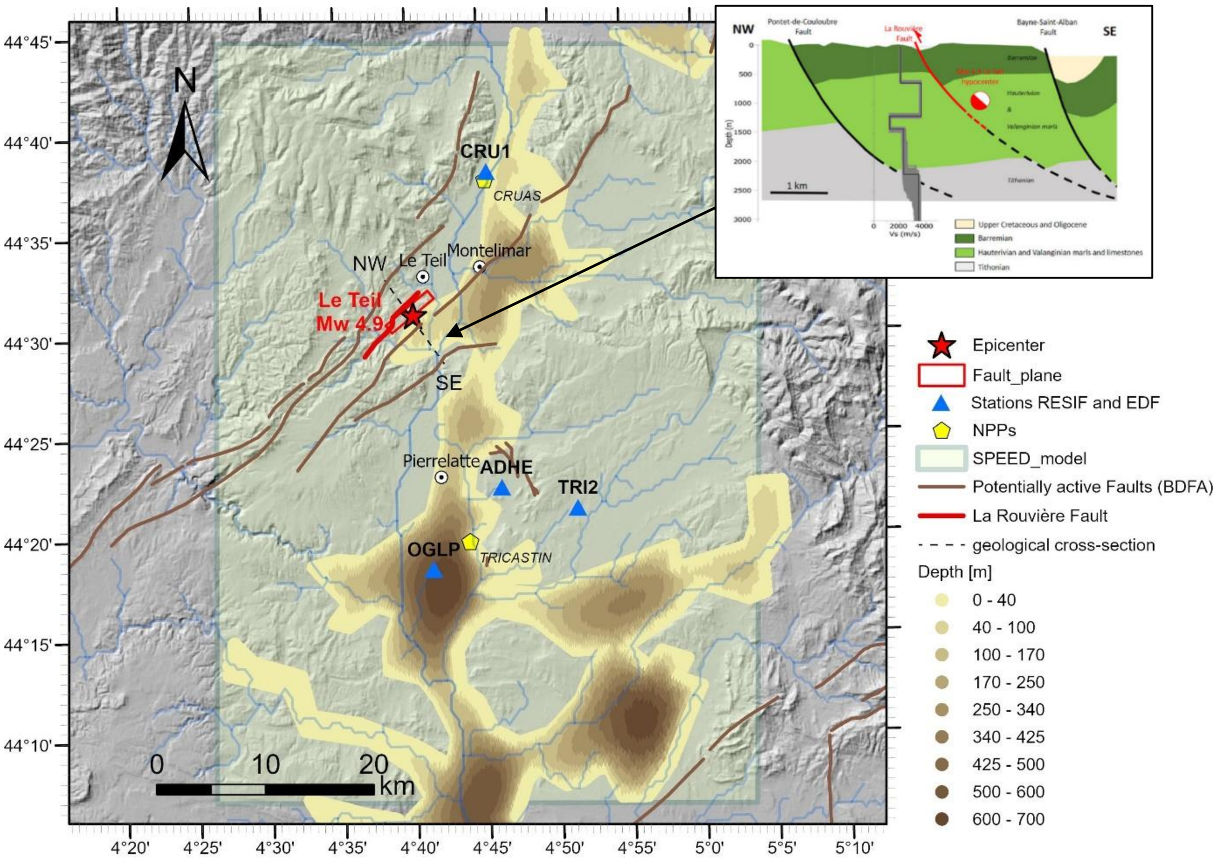

Figure 2. Basin model used in numerical simulations. Fault and epicenter of the earthquake (in red) are shown with indication of the extent of the SPEED model (superimposed transparent yellow box). The location of recording stations (blue triangles) as well as the two nuclear power plants (Cruas and Tricastin, yellow hexagons) are shown. In the legend, 'Depth' is measured from local topography. The brown lines are potentially active faults from the BDFA catalogue (https://bdfa.irsn.fr/), while the La Rouvière Fault (LRF) is marked in red. The inset on the top right corner (from Causse et al. 2021) shows the NS-EW geological cross-section modified from Ritz et al., 2020 (licensed under CC BY 4.0.).

3.1 Set-up of the 3D velocity model of the Rhône River Valley

The construction of the 3D subsoil model of the region implied some preliminary analyses to properly identify the main features of the Rhône Valley and of the seismic wave velocity model for both the crustal layers and the sedimentary materials within the valley. In particular, the limited geophysical and geological information at large-scale required to develop a numerical algorithm to shape a preliminary 3D model of the Rhône Valley, constrained on the sparse data made available.

Namely, the 3D model of the Rhône Valley shown in Figure 2 was constructed from numerical processing of the information included in the DEM (Digital Elevation Model) of the area, available at https://download.gebco.net/, with a resolution of 300 m, further constrained by the sediment depth from available geological cross-sections and by the surface contour of outcropping sediments. For this purpose, an ad hoc algorithm was developed, providing an estimate of the local depth of the Rhône Valley sediments, based on the equilibrium of an elastic and homogeneous membrane fixed at the valley boundaries (i.e., Poisson equation), subjected to a distributed loading inversely proportional to the distance of the point from the boundary. Further details of the procedure are provided in El Haber et al. (2022).

As noticeable from Figure 2, the valley shape and depth change considerably, being narrow and shallow in the North, close to Cruas NPP, and large and relatively deep in the South, close to Tricastin NPP. The maximum sediment thickness reaches about 700 m near the OGLP station.

The velocity model of the deep crustal layers implemented in the numerical model (Table 2), was borrowed from Causse et al. (2021), who performed a set of numerical simulations of the Montélimar earthquake and characterized for that purpose the 1D structure of the earth crust using seismic noise recorded at temporary seismological stations installed after the earthquake in the fault vicinity. These profiles, in the epicentral area, exhibit soil materials with increasing stiffness from the surface to 1.2 km depth, overlaying less competent deposits (see the geological cross section in Figure 2). As remarked by Causse et al. (2021), this inversion in the velocity profile is consistent with the geological settings of the area (Elmi et al., 1996) and with information from deep boreholes in the region.

Table 2. Crustal model used in numerical simulations. Adapted from Causse et al. (2021). ρ is the soil density, V_P and V_S are the P- and S-wave propagation velocities, respectively.

Thickness [m]	ρ [t/m^3]	V_P [m/s]	V_S [m/s]
600	2.0	3400	2100
600	2.5	5800	3500
220	2.2	2000	1200
780	2.4	3900	2300
6000	2.5	5800	3500

Concerning the sediments, a seismic velocity model was calibrated based on the measured profiles available at the OGLP station (RAP-ID project, Regnier et al., 2010) and at the Tricastin NPP (from local investigations carried out at the moment the NPP was under construction, EDF personal communication). Other profiles north of Montélimar, around the NPP of Cruas (at CRU1 station), at the border of the basin, were used for verification. Based on this information, a parabolic V_S and V_P profile were defined as a function of the depth from the topographic surface (*z*), as follows:

$$V_S(z) = 300 + 53.7 \cdot z^{0.5}; \quad V_P(z) = 550 + 78.3 \cdot z^{0.5} \tag{1}$$

For soil density, a constant value ρ=1950 kg/m^3 was chosen, in agreement with available data. The adopted V_S model (Eq. 1) is shown in Figure 3 (black line), together with the measured profiles and the crustal model of Table 2 (dashed brown line). Note that, for sake of simplicity, the velocity profile is homogeneous along horizontal plans in the basin. At the generic point in the basin, the Vs profile consists of Eq (1) until the depth of the basin is reached and then, beyond that depth, the crustal model applies.

Concerning anelastic attenuation properties, for all soil layers, a frequency-dependent quality factor ($Q=Q_0*f/f_0$) was adopted, with $Q_0 = V_S/10$ and a reference frequency f_0 = 1 Hz.

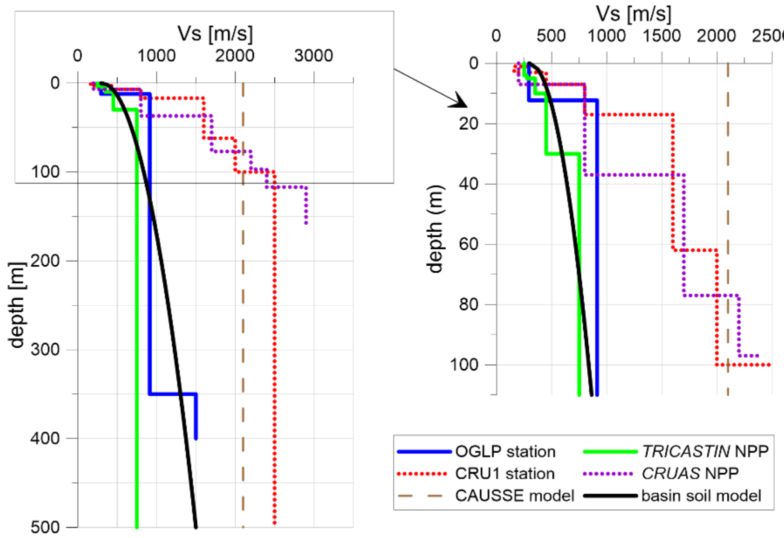

Figure 3. V_S profiles available at different sites within the Rhône Valley. The adopted surrogate model, calibrated on OGLP and Tricastin NPP, is shown in black and it is applied until the bedrock depth is reached.

3.2 *Kinematic seismic source model*

A kinematic representation of the fault rupture process was adopted to model the seismic source of the Le Teil earthquake. In spite of the moderate magnitude, a finite-fault modelling was preferred to point-source to provide more realistic ground motion predictions in the near-source region.

Among the studies devoted to the inversion of a kinematic model of the seismic source (Delouis et al., 2019; Cornou et al., 2021; Ritz et al., 2020; De Novellis et al., 2020; Mordret et al., 2020), the one proposed by Cornou et al. (2021) was adopted, in agreement with the partners of the SIGMA-2 Project. It is obtained from inversion of Interferometric Synthetic Aperture Radar (InSAR) images acquired by the Sentinel-1 satellite. The used kinematic source parameters are summarized in Table 3, while the co-seismic slip distribution on the fault plane and the Slip Rate Function (SRF), in both time and frequency domain, are illustrated in Figure 4. The SRF is defined according to Crempien and Archuleta (2015), assuming a rise time τ equal to 0.5 s.

Following Causse et al. (2021), a constant rupture velocity, V_R = 1800 m/s, was adopted, corresponding to 85% of the shear wave velocity of the top layer of the crustal model.

Table 3. Main kinematic source parameters used in the simulations. The Cornou et al. (2021) solution is the reference fault model.

Parameter	Cornou et al. (2021)
M_W	4.9
Epicenter location	44.521°N; 4.669°E
Hypocenter depth [m]	1000
Source area [km^2]	5000 x·1740
Rupture velocity V_R [km]	1800
Strike [°]	50
Dip [°]	58
rake [°]	89
Co-seismic slip	See Figure 4

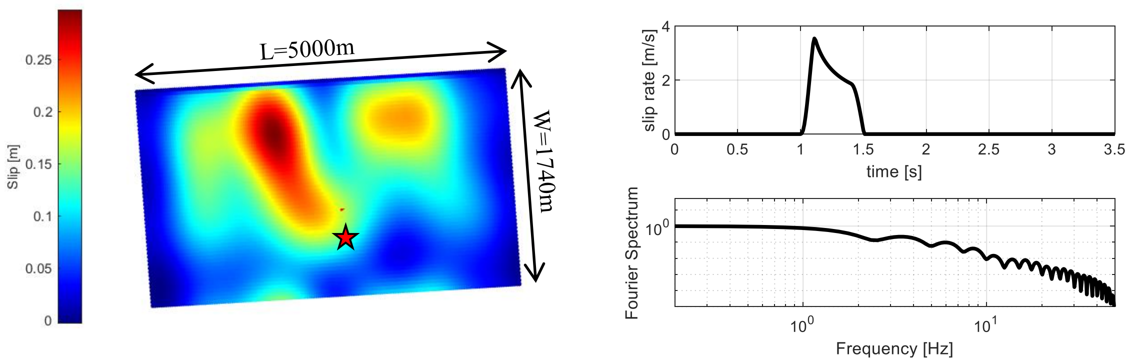

Figure 4. Left. Adopted co-seismic slip distribution (from Cornou et al., 2021) and position of the hypocenter (red star). Right: Slip Rate Function in time and frequency domain (from Crempien and Archuleta, 2015), with rise time = 0.5 s.

From a computational point of view, it is worth highlighting that the source modelling in SPEED takes advantage of a novel strategy, referred to as “not-honoring fault” (see Sangaraju et al. 2021, for the simulation of the 2016 Kumamoto earthquakes), specifically developed to account for finite-fault rupture models with arbitrarily complex geometries in a numerically efficient way. According to this approach, the mesh design does not need to incorporate the geometry of the fault plane (making the meshing operations time-consuming and source-specific), but spectral nodes approaching the target fault rupture area are searched and loaded in order to reproduce the total seismic moment of the event to be simulated.

3.3 Mesh computational features

Figure 5 illustrates the 3D spectral element numerical model, with indication of the finite-fault source area and the surface marking the boundary between the basin sediments and the underlying bedrock. The numerical domain extends over a volume of 45 km × 70 km × 8.5 km and it is discretized using a structured conforming hexahedral mesh with average length of the spectral elements ranging from about 120 m, at ground surface, to 550 m, at the bottom of the model. Referring to Section 4.2 for quantitative tests on the accuracy of the numerical solutions in the high-frequency range, the mesh was found to propagate accurately frequencies up to about 8 Hz. Using a fourth-order spectral polynomial degree (SD=4), the total number of spectral nodes amounts to more than 80 millions. Due to the large number of degrees of freedom, numerical simulations were performed on the Marconi 100 Cluster at CINECA, the largest high-performance computing center in Italy (www.cineca.it). The walltime for each numerical simulation is around 3 hours on 128 cores of the Marconi 100 cluster, leading to a computational cost of almost 400 cores-hours.

Table 4 provides an overview of the numerical simulations that were performed in this study with the aim of (i) verifying the numerical simulation and (ii) testing the impact of the 3D model effects on ground motion. With reference to (i), a simpler numerical mesh, with flat topography and crustal 1D layered structure was built.

Table 4. Overview of the numerical simulations by SPEED.

Label	Topography	Soil Model	Source	Slip Model
1D-pt	Not included	Crustal (1D)	Point-Source	Not used
3D-C21	Included	Crustal with Basin	Finite-Fault	Cornou et al.
3D-C21-R	Included	Crustal without Basin	Finite-Fault	Cornou et al.

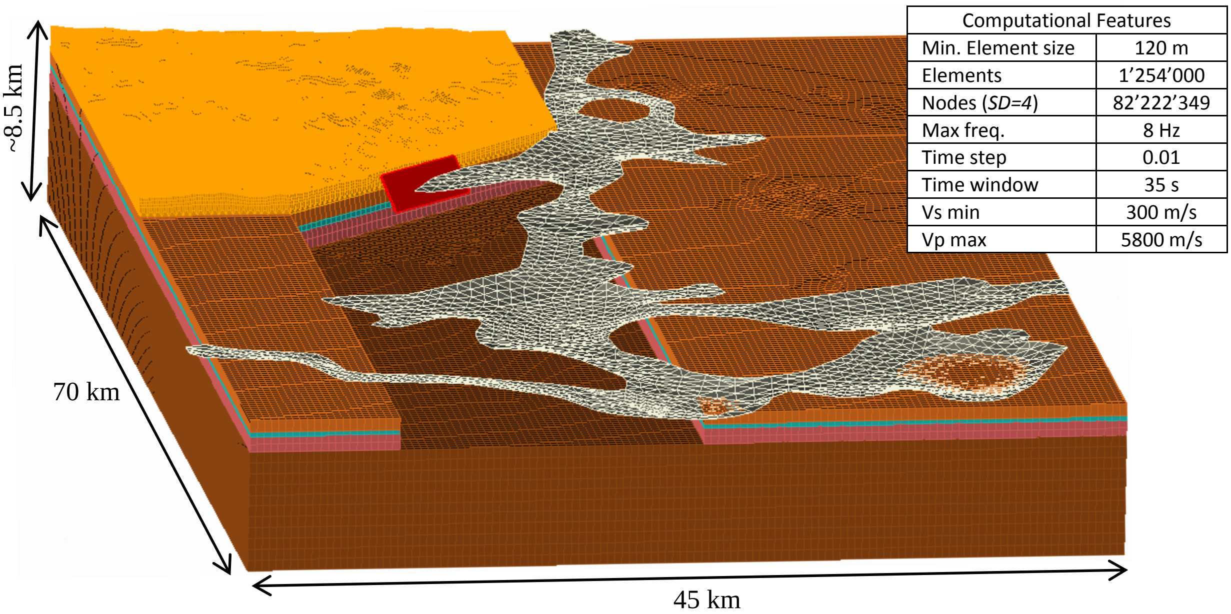

Figure 5. Overview of the 3D numerical model: basin structure, crustal layering and numerical fault (in red). Details of the computational features are given in the table on the upper left corner.

4 Verification tests

4.1 Verification analyses with Hisada code

As a preliminary step of the modelling procedure, simulations were performed using the Hisada code, based on the analytical integration of Green's functions (Hisada and Bielak, 2003). This code allows to compute the ground motions in a horizontally layered half-space originating from a finite-fault kinematic source model, providing solutions with a maximum frequency resolution of about 1-2 Hz at most.

Hisada's solution has been used in a preliminary phase to calibrate and validate the crustal model profile, the assumptions on the quality factor, the slip model on the extended fault and the source time function adopted. Concerning the source, two different parametrizations have been tested: a point source (shown herein) and an extended fault (not shown in this paper). The simplified numerical model, without the basin shape and with the 1D crustal layering and flat topography, has been used for these tests (1D-pt model of Table 4).

Figure 6 shows the recorded and simulated velocity time histories and corresponding Fourier amplitude spectra (FAS) obtained from SPEED and from Hisada's approach at station CRU1 and at a virtual receiver located at about 1 km from the source. All time histories have been low-passed filtered at 3 Hz, given the low frequency resolution of Hisada solution. Herein a simple point-source model is adopted with an exponential source time function (rise time τ=1.2 s), for consistency with the built-in source functions available in Hisada code. An excellent agreement between the two simulation techniques is found, especially in the near source, proving the accuracy of the numerical mesh. Agreement with recorded time series is good as well, both in amplitude, frequency content and arrival times. A detailed discussion on the misfit between simulations and recordings, in a broader frequency range, will be addressed in Section 5.

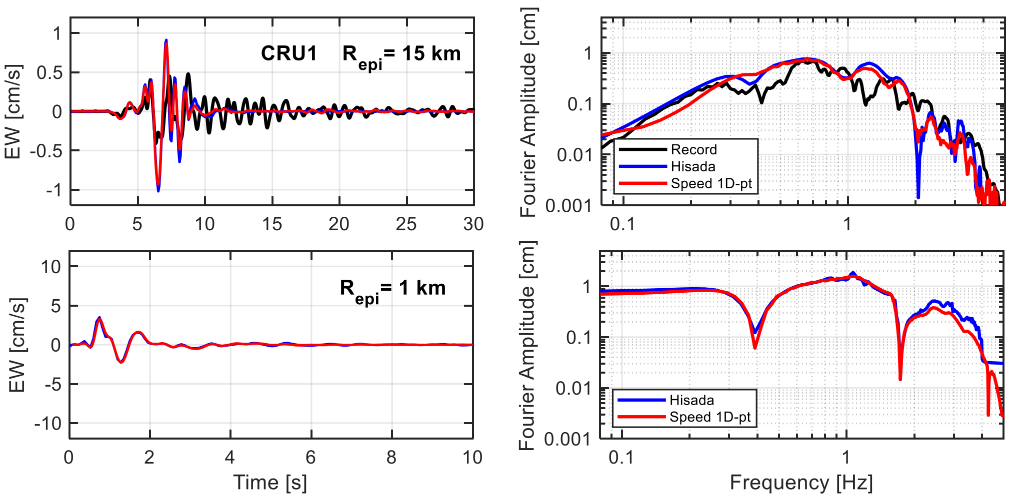

Figure 6. CRU1 station (R_{epi}=15 km, top) and a near field receiver (R_{epi}=1 km, bottom). Simulated (and recorded, where available) velocity time histories and corresponding Fourier Amplitude spectra for EW component. Point source 1D model, with flat topography and horizontal layers (1D-pt in Table 4). All time histories are low-pass filtered at 3 Hz.

4.2 Numerical accuracy in the high-frequency range

Among the various approaches for numerical integration of the linear-elastodynamic wave equations, the spectral element approach enjoys a high accuracy, referred to as spectral accuracy, that was estimated to ensure an accurate wave propagation with slightly more than the Nyquist limit of 2 points per minimum wavelength (ppmw) for homogeneous soil conditions, up to about 4 ppmw in strongly heterogeneous materials (Faccioli et al., 1997). These estimates were based on verification tests on closed-form and/or reference solutions from literature. For a practical application, a proper check of the number of ppmw should be made for the specific case study, depending on the desired accuracy. For this purpose, a convergence test was performed considering the numerical model described in Section 3.3 (model 3D-C21 of Table 4), where, with the same discretization in terms of spectral elements, the spectral degree (SD) of each element was increased from SD=1 (i.e., no internal Legendre-Gauss-

Lobatto (LGL) node is present along each edge of the spectral element) up to SD=5 (i.e., six LGL nodes within each side of the spectral element). In this way, the accuracy of the solution for SDj (j=1, 2…5) can be checked by verifying at which frequency it departs significantly from the solution obtained with SDj+1. Results of this test are illustrated in Figure 7, showing that, taking as a reference SD5, the solution with SD4 keeps close to SD5 up to about 7.5 Hz on outcropping bedrock and up to about 5 Hz on outcropping basin. These should be considered as the reference accuracy limits of our numerical results when comparing them with records.

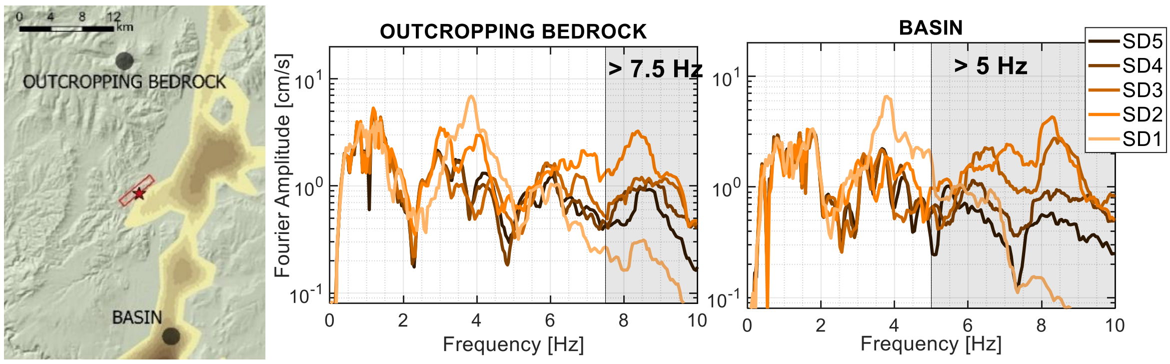

Figure 7. Fourier amplitude spectra simulated (3D-C21 model of Table 4) for varying Spectral Degrees (SD from 1 to 5) at two positions at about 17 km from epicenter: on outcropping bedrock (to the North) and on soil (to the South), inside the basin.

However, it should also be pointed out that neither the input slip function nor the numerical model are detailed enough at high frequencies, which are dominated by small-scale effects of stochastic nature. As it will be shown by comparing numerical results with records, the high-frequency decaying trend of simulated Fourier spectra is consistent with that of records. Because of such good agreement, we discarded the option to produce broadband results by coupling the low-frequencies from PBS to the high-frequencies produced by either stochastic methods or by Artificial Neural Network-ANN, such as proposed by Paolucci et al. (2018). Indeed, such hybrid approaches may not be theoretically well constrained for very shallow events, as it is the case of Le Teil earthquake. Moreover, in the case of ANN, a sufficient amount of records is necessary for training, which is not available for such shallow focal configurations. For this reason, we considered more physically sound to rely on the numerical content of the signal up to about 8 Hz (i.e., signals were LP filtered below 10 Hz). Indeed, although affected by a moderate dispersion, we verified that, in the selected frequency range, the resulting wavefield retains realistic characteristics in terms of amplitude, duration and spatial correlation, that would be lost by LP filtering.

5 Overview of simulated results and comparison with records

In this section a summary of the final simulations is given, comparing results from the 3D-C21 model of Table 4, with recordings and empirical GMMs, over the whole numerical domain.

5.1 *Velocity motion and ground shaking maps*

In Figure 8, snapshots of horizontal ground velocity in the EW direction are shown, illustrating the patterns of seismic wave propagation and its interaction with the Rhône Valley. Basin induced amplification is noticeable both near the source, in the shallower portion of the basin, to the East of Montélimar (see snapshot at 7 s), and in the deeper Southern portion of the basin, such as near the OGLP station (see snapshots at 11 s).

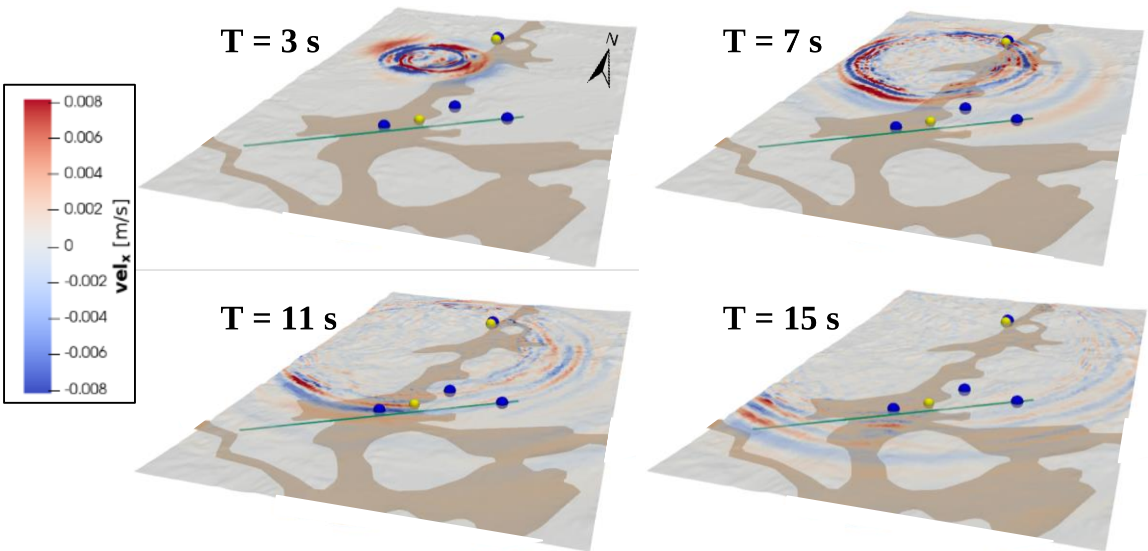

Figure 8. Snapshots of EW simulated velocity (model 3D-C21) at 3, 7, 11 and 15 s. The basin shape is shown together with the stations (blue dots) and the NPPs (yellow dots). The green line is the cross-section along which basin amplification effects are studied in Section 6.

Figure 9 shows ground shaking maps of peak ground displacement (PGD), velocity (PGV) and acceleration (PGA) for vertical and horizontal components rotated in the strike fault normal (FN) and fault parallel (FP) directions. Recordings are shown as well, at reference stations, using the same palette. Simulated and recorded ground motions are filtered with a low-pass filter at 10 Hz. The maps of Figure 9 point out an intense ground shaking in the immediate vicinity of the main rupture area, both in horizontal and vertical direction. The maps provide also a clear picture of the radiation pattern associated with a reverse focal mechanism and its interaction with complex subsurface geology. Up-dip directivity effects are visible on the hanging wall of the fault, yielding to a significant increase of ground motion amplitude, with maximum PGA, PGV and PGD values up to 2.5 m/s^2, 0.4 m/s and 0.1 m, respectively. Two prevailing directions of polarization of maximum amplitudes are noted, at azimuths of around 45° and 270° measured clockwise from North, most likely because of the influence of the two shallow slip asperities (see Figure 4) on radiation pattern and directivity effects. The influence of the basin sediments is clearly noticeable, although limited in amplitude, especially in the PGA map. Vertical motions are high especially above the main slip area, with peak amplitudes which are comparable or even larger than the horizontal ones, consistent with observational evidences of large vertical-to-horizontal ratios in near-source conditions (Ramadan et al. 2021). FN and FP components show comparable amplitudes, although FN components tend to be larger than the FP ones on the surface projection of the fault rupture area.

In general, the maps indicate a realistic spatial correlation structure of peak ground motion values, in a wide frequency range (from PGD, at low frequency, to PGA, at larger frequencies): as expected, PGA shows a more significant contribution of small-scale spatial variability than PGV and PGD. Agreement with peak values of recorded motion is considerable, mostly in the horizontal directions.

Although not shown herein for sake of brevity, the simulated permanent vertical displacement on the surface projection of the fault plane (see, as a proxy for the spatial distribution of permanent ground uplift, the PGD –UD map in Figure 9, bottom-right) reaches maximum values of about 10 cm, in reasonable agreement, although underestimated, with the maximum uplift of 15 cm from InSAR measurements (Ritz et al. 2020).

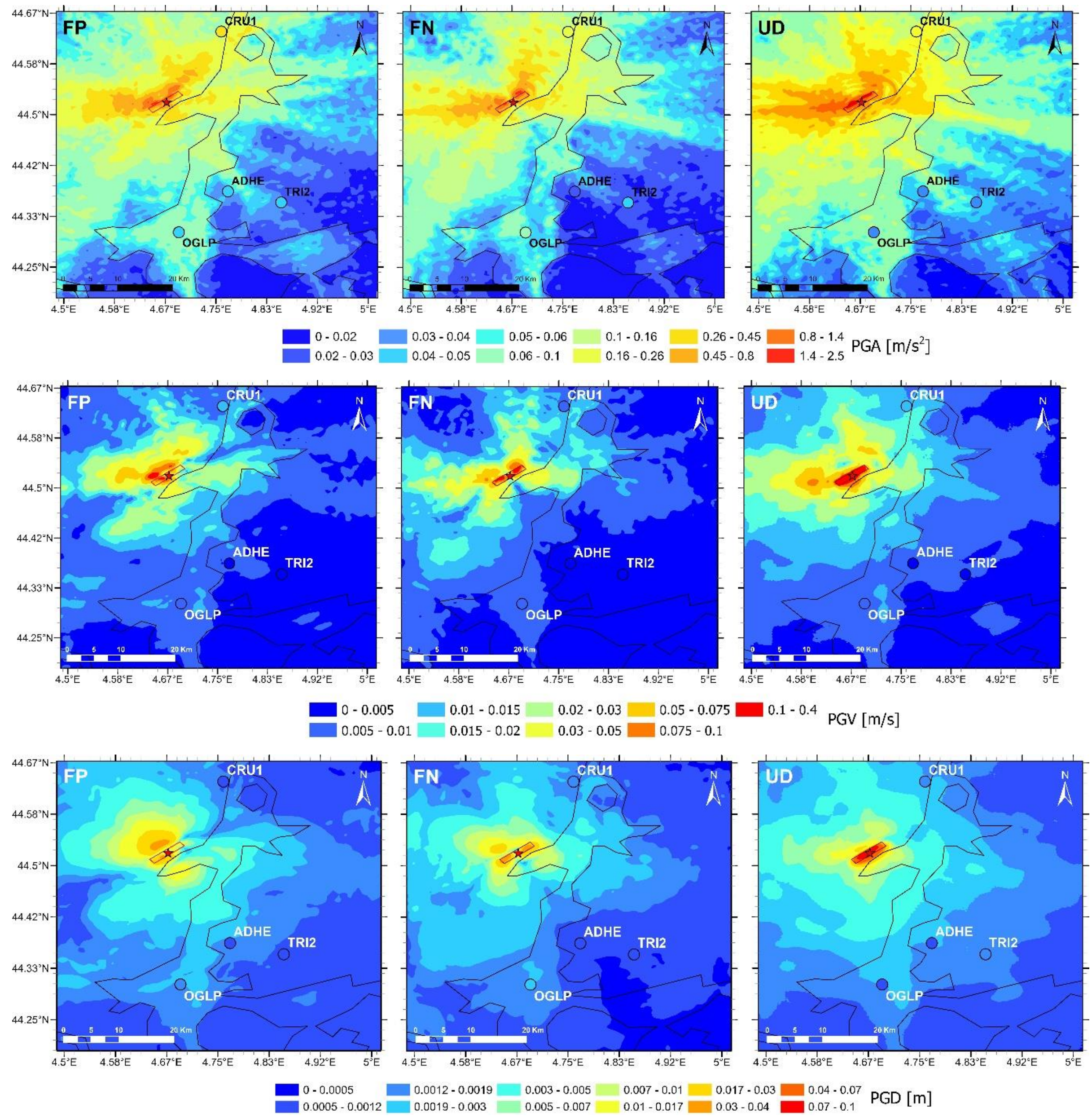

Figure 9. PGA (top), PGV (middle) and PGD (bottom) maps from simulation 3D-C21. Recorded peak values are shown with colored circles. Le Teil earthquake fault (red rectangle) and epicenter (red star) are shown as well.

5.2 Detailed comparison in time and frequency domain

Figure 10 (a and b) compares recorded ground motion with SPEED simulations, at the four stations: (a) CRU1, on the basin edge to the North-East of the epicenter, and OGLP, inside the basin, and (b) ADHE and TRI2, on outcropping bedrock to the South-East of the epicenter. Comparisons are shown in the time and spectral domain. For all stations, simulations are in satisfactory agreement with recordings in terms of amplitudes, arrival times and duration of motion. The vertical component tends to be in general more amplified, especially on later arrivals, both on bedrock and soil. At outcropping bedrock stations, ADHE and TRI2, simulations show on average a lower agreement with respect to other stations; being on the other side of the basin, with respect to the source, they are more sensitive to the shape and basin properties (simplified in this work as explained in Section 3.1). Inside the basin (at OGLP station), simulations are in very good agreement with observations for the main phases of ground motion, even though, in the horizontal direction, recordings exhibit reverberations with stronger amplitudes, not captured by the simulation. It is interesting to note that the simulations turn out to reproduce relatively well the high energy content of vertical motion at long periods (larger than 0.5 s, note in particular long period branch of CRU1 and OGLP spectra). This is a peculiar feature of the Le Teil earthquake, whose recordings indicate vertical-to-horizontal ratios significantly larger than those predicted by up-to-date empirical models at long periods (Ramadan et al. 2022).

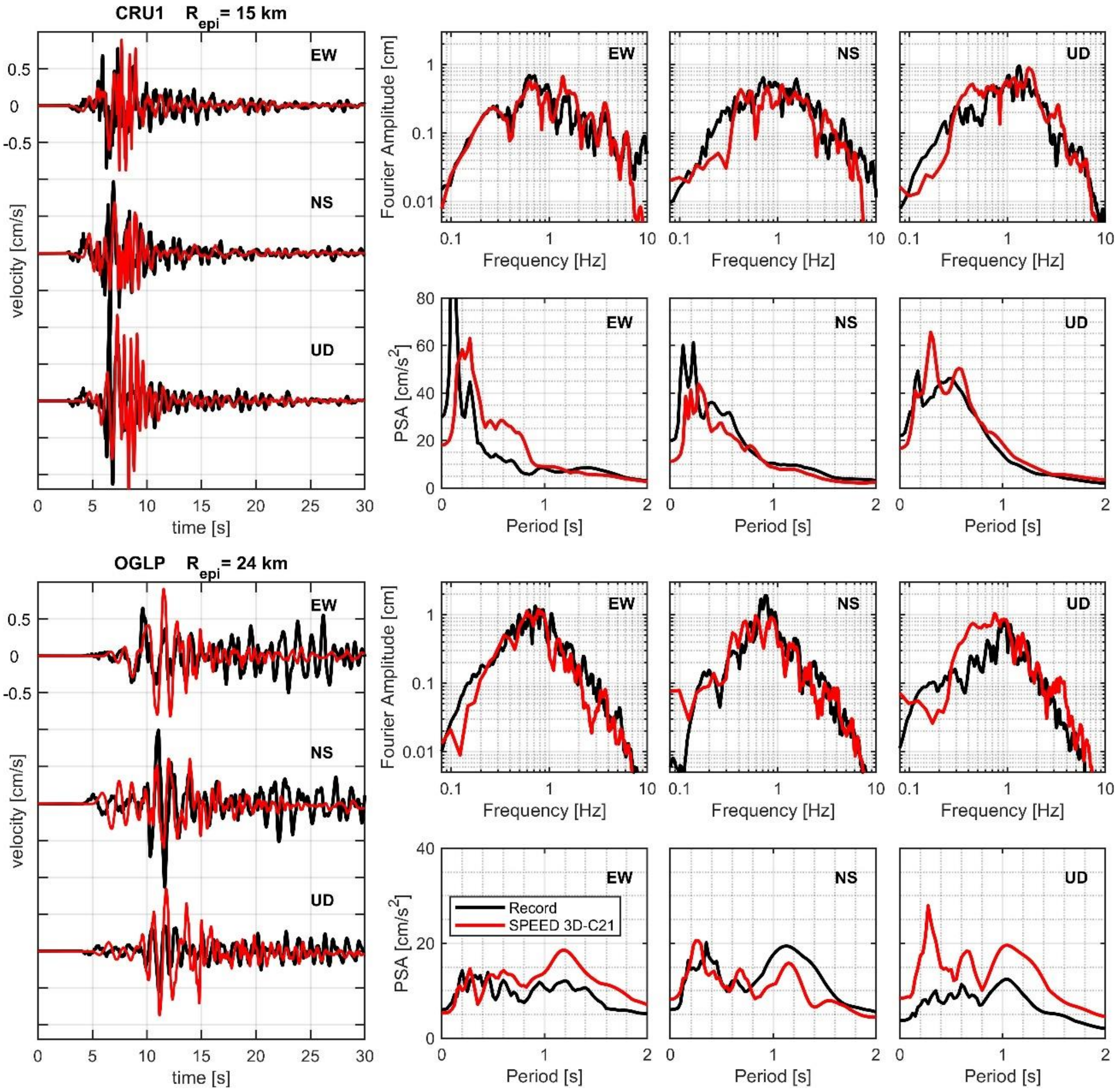

Figure 10 a. CRU1 (R_{epi}=15 km) and OGLP (R_{epi}=24 km) stations. Simulated (red, 3D-C21 model) and recorded (black) velocity time histories with corresponding Fourier and Response spectra. All time histories are low-pass filtered at 10 Hz.

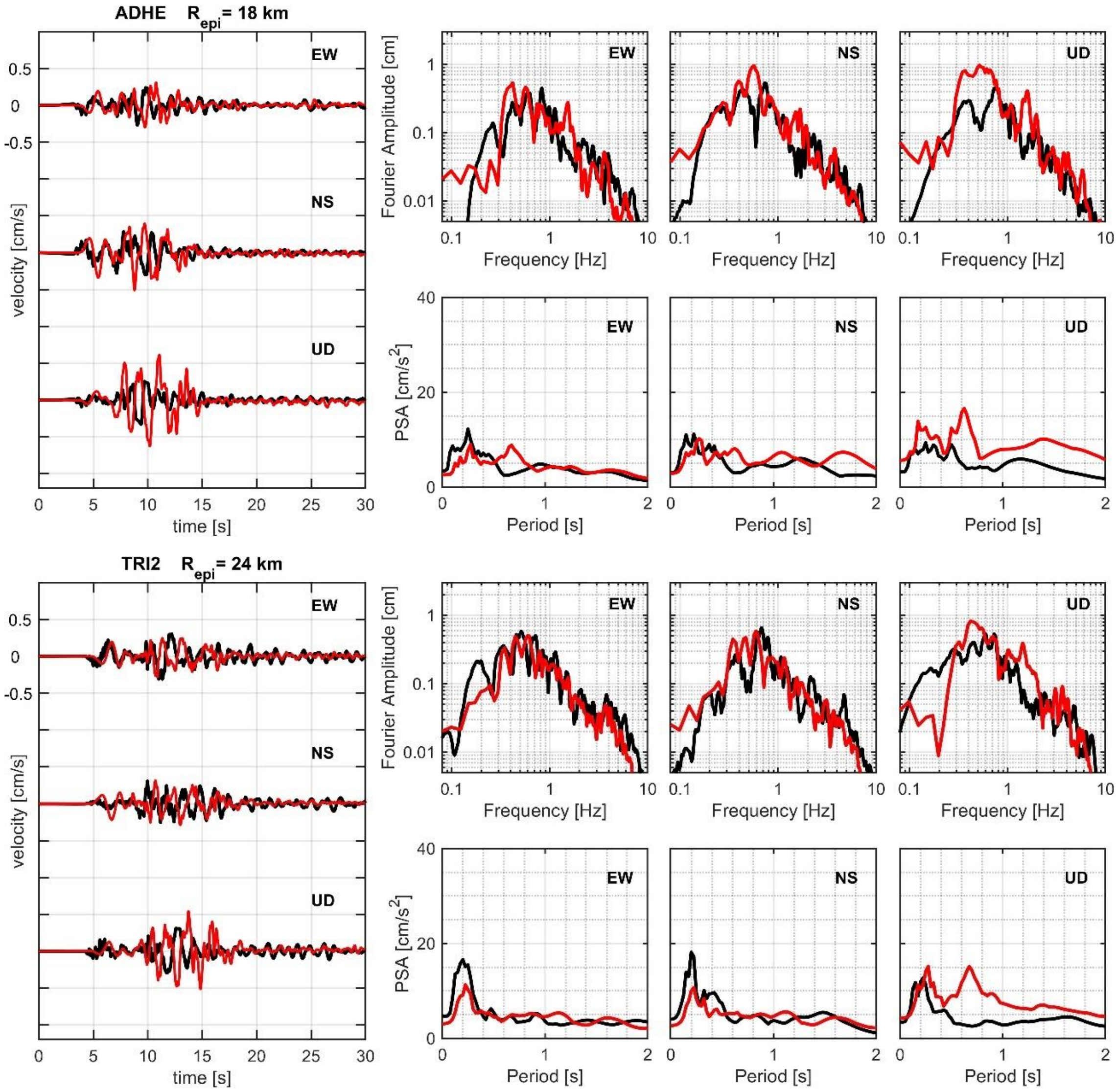

Figure 11 b. Same as Figure 10 a, for ADHE (R_{epi}=18 km) and TRI2 (R_{epi}=24 km) stations.

5.3 Goodness-of-Fit Scores

The overall performance of the numerical simulations was quantitatively estimated through the Goodness-of-Fit (GoF) criteria proposed by Anderson (2004), considering ground motion parameters of interest for earthquake risk applications, namely: Peak Ground Acceleration (PGA), Peak Ground Velocity (PGV), Peak Ground Displacement (PGD), Acceleration Response Spectra (SA) at selected periods (T = 0.2, 0.5, 1 and 2 s) and Cumulative Absolute Velocity (CAV). Figure 12 shows the individual scores associated with the aforementioned parameters for the set of four reference stations, for both horizontal geometric mean (GMH) and vertical (UD) components. An overall good-to-excellent agreement is found for the horizontal components for all stations and all parameters. For the UD component, slightly worse scores are found, probably due to the higher frequency content of the vertical motion. The closest station (CRU1) shows the best performance on the vertical component.

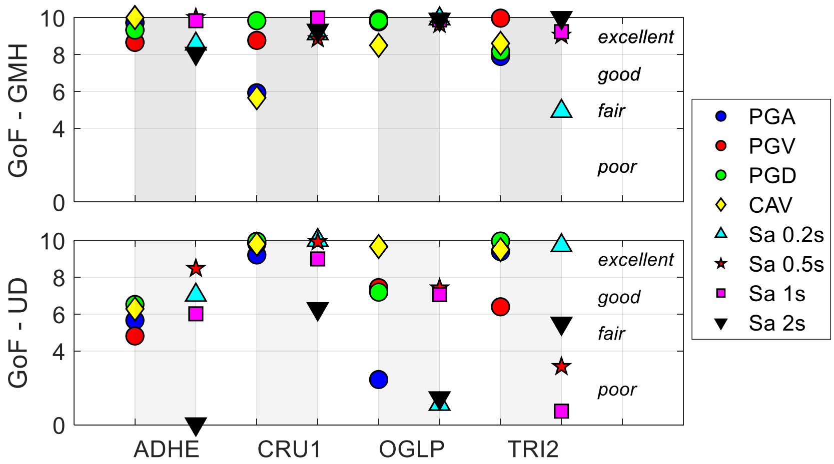

Figure 12. GoF scores computed on PGA, PGV, PGD, SA at T = 0.2, 0.5, 1.0 and 2.0 s, and CAV, for both GMH and UD components. Simulations performed with the 3D-C21 model of Table 4.

5.4 Ground motion attenuation with distance

Figure 13 shows horizontal PGA, SA(0.2s), SA(0.5s) and SA(1s) as a function of Joyner-Boore distance, R_{jb}, from 3D-C21 SPEED simulations (black: on outcropping bedrock; grey: inside the basin) as well as from recordings (green circles) and from the GMM by Kotha et al. (2020) for shallow crustal events (violet: rock, with V_{S30}=2100 m/s; red: basin, with V_{S30} =500 m/s), in its ergodic formulation. V_{S30} values of empirical predictions are selected to be consistent with the Vs profiles implemented in the numerical model. For both simulations and recordings, the median (RotD50) values of spectral accelerations over all orientations (Boore, 2010) are considered for consistency. The same comparison is shown in Figure 14 but for the vertical component, using as the GMM by Stewart et al. 2016.

These comparisons suggest that:

- numerical simulations are suitable to fill in the gap left by the recordings in the proximity of the seismic source: while the records cover, with a very limited sampling, only distances beyond about 15 km, numerical simulations provide a detailed picture of ground motion in the near-source region (0-15 km), with relevant implications for constraining the seismic input for the NPPs;
- in general, in the distance range between 15 and 25 km, the agreement between simulated and recorded spectral values is satisfactory, since no systematic biases are

found. Some discrepancies are found at CRU1 station, especially for the horizontal PGA and vertical SA(0.5s);

- simulations suggest a tendency of near-source ground motions to be lower than the GMMs model at short periods (particularly for PGA), while a reverse trend is found at long periods (≥1.0s), where simulated ground motions exceed significantly the empirical predictions. Such a trend is consistent with the findings from residual analysis of Montélimar recordings with respect to recorded datasets in Europe and in Italy;
- the systematic underestimation of the empirical GMMs for the long-period spectral ordinates is even more pronounced for the vertical components of ground motion, for which both simulations and recordings tend to be systematically above the 84th percentile of the empirical predictions;
- at intermediate periods (see SA(0.5s)-H and SA(0.2s)-V) a better agreement is found between numerical simulations and empirical predictions.

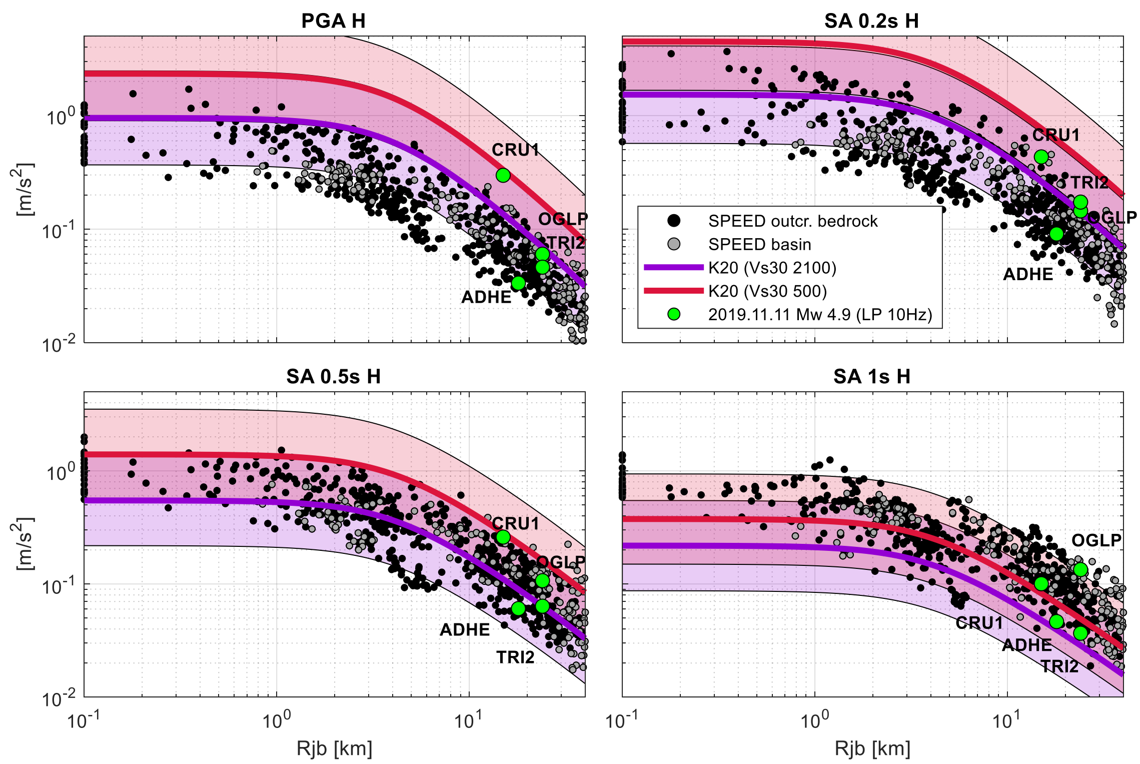

Figure 13. Horizontal (RotD50) acceleration spectral values (PGA, 0.2 s, 0.5s, 1 s) as a function of Joyner-Boore distance Rjb, from recordings (green circles), 3D-C21 simulations (black dots: outcropping bedrock; grey dots basin) and from Kotha et al. 2020, K20, (median and ± 1 standard deviation as shaded regions, violet for V_{S30}=2100 m/s, red for V_{S30}=500 m/s).

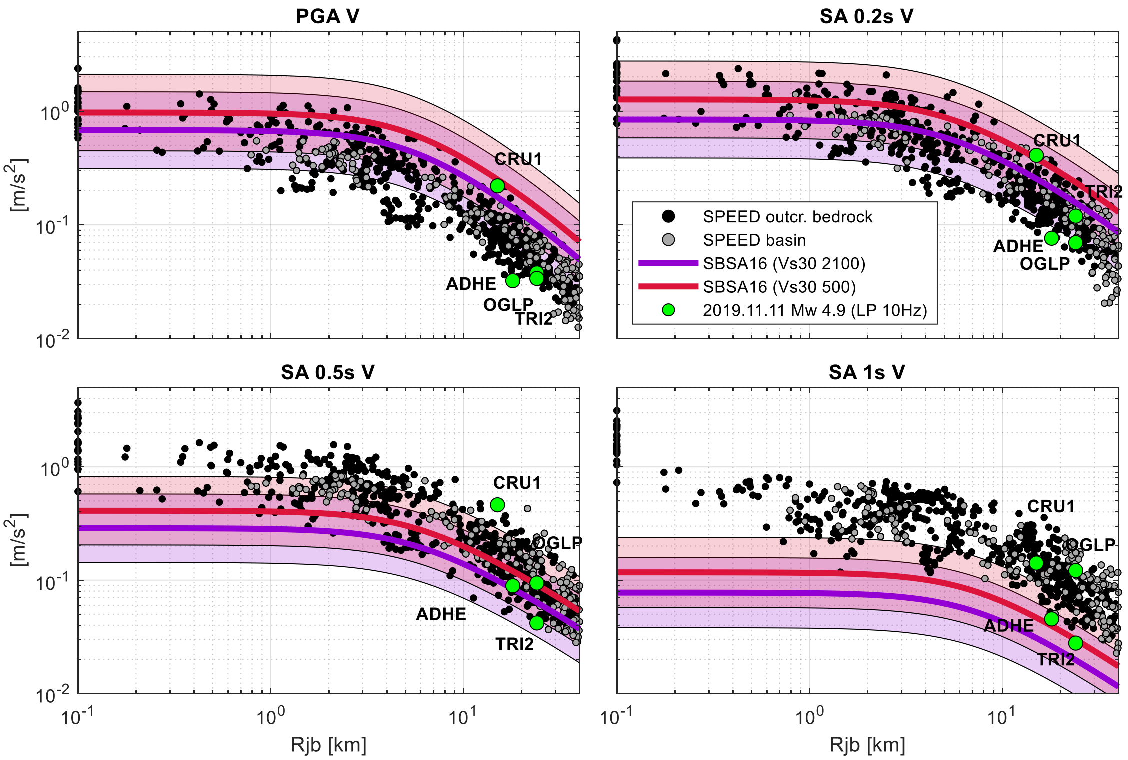

Figure 14. Same as Figure 13 for the vertical component of acceleration and the Stewart et al. 2016, SBS16, ground motion attenuation relationship.

6 Basin amplification effects

One of the main advantages of PBS is that, unlike for records, site conditions are completely known. While the complexity of the small-scale variability of ground properties cannot be portrayed in detail, unless spatially correlated stochastic fields are applied to the average values of wave propagation velocities (see Paolucci et al., 2021, for an application to the PBS of ground motions from induced seismicity in Groningen, Netherlands), PBS are suitable to investigate site amplification effects from a variety of viewpoints, such as: (i) the variability of site amplification with respect to different outcropping bedrock stations; (ii) the comparison with the results from 1D and 2D simulations (see e.g. Smerzini et al., 2011, for an application to the Gubbio basin, Italy); (iii) their repeatability and scenario dependence both in the linear and non-linear ranges (see e.g., Stafford et al., 2017). Although SPEED allows for consideration of a relatively simple, albeit effective, non-linear visco-elastic model (Stupazzini et al., 2009), due to the relatively low levels of seismic excitation we will consider in this section only linear visco-elastic site amplification effects. To this end, the focus is on the cross-section shown in Figure 15 (the azimuth of the cross-section is the same as the fault strike), where, velocity time histories at selected locations, are illustrated, on the top panel, both in the basin and at outcropping bedrock, and, on the bottom, at all receivers along the cross-section (the EW component was chosen as reference for these investigations, for simplicity). The latter plot allows to highlight the complexity, as well as the 3D nature, of seismic wave propagation in the basin. As clarified also from Figure 8, the western portion of the cross-section is the one that first experiences ground motion due to the lower source-to-site distance, but afterwards the presence of the basin increases the complexity of the overall seismic wave field, with prominent amplification effects towards the basin center.

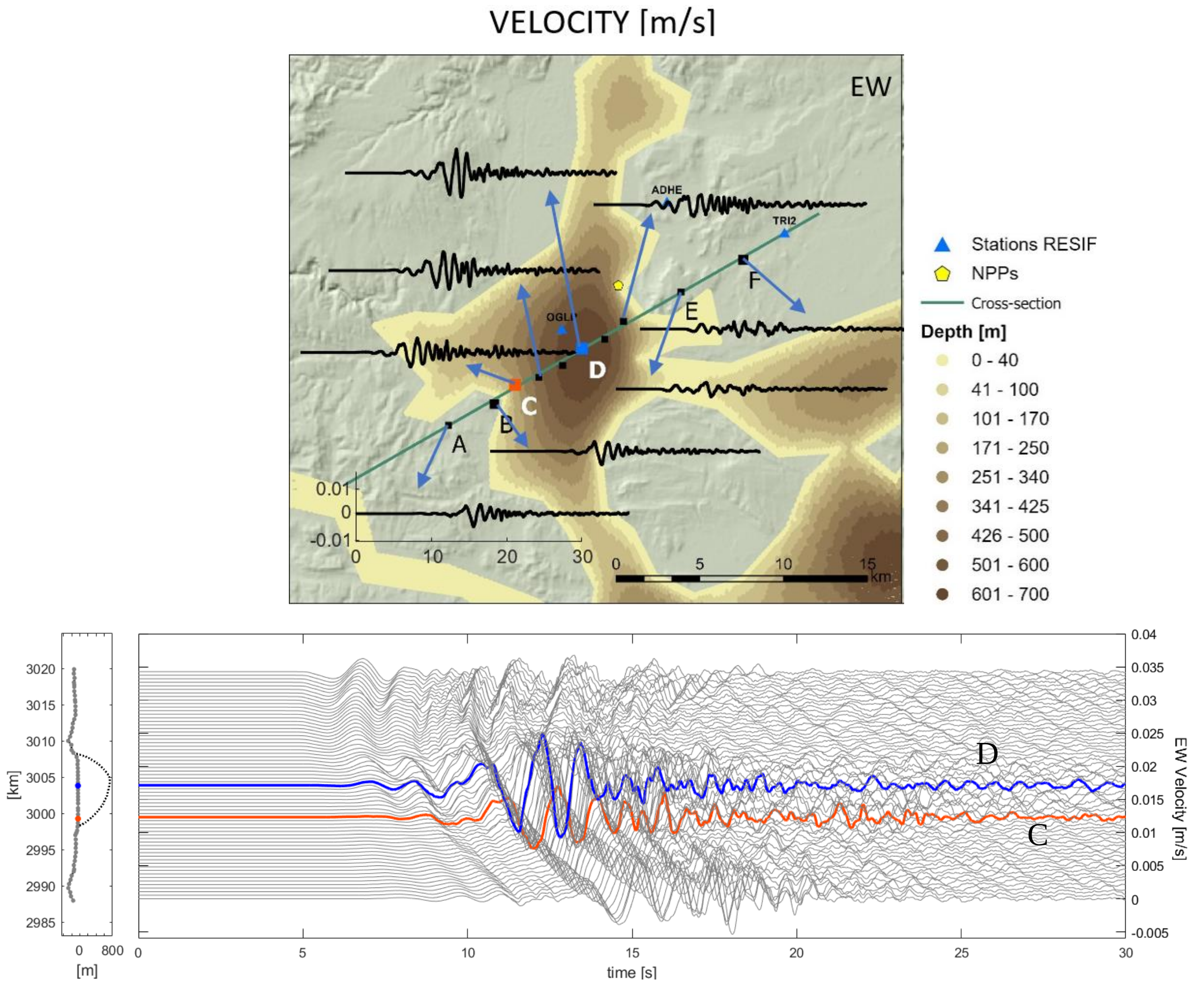

Figure 15. Top: sketch of the southern portion of the Rhône basin, with the studied cross-section passing in the vicinity of the OGLP station and Tricastin NPP. Time histories of EW velocity at selected receivers along the cross section are shown. Bottom: EW velocity time histories along the same cross section. Two receivers inside the basin are highlighted, denoted by C (red line) and D (blue line). Simulations resulting from the 3D-C21 model of Table 4.

To quantify the basin-induced amplification, regardless of the reference station, a second PBS, with the same reference kinematic source model (see Section 3.2), was carried out but without the presence of the basin. In such simulation, referred to as "3D-C21-R" (where "R" means "rock") in Table 4, the dynamic properties of the basin are replaced by those of the outcropping bedrock. In Figure 16 (left), the acceleration time histories at D and C receivers (shown in Figure 15) are plotted, clearly pointing out the increased amplitude, and elongated dominant period and duration of ground motion with respect to the case without basin. Such prominent amplification is clearly shown in terms of the corresponding acceleration response spectra, highlighting the significant long period amplification especially at the center of the basin.

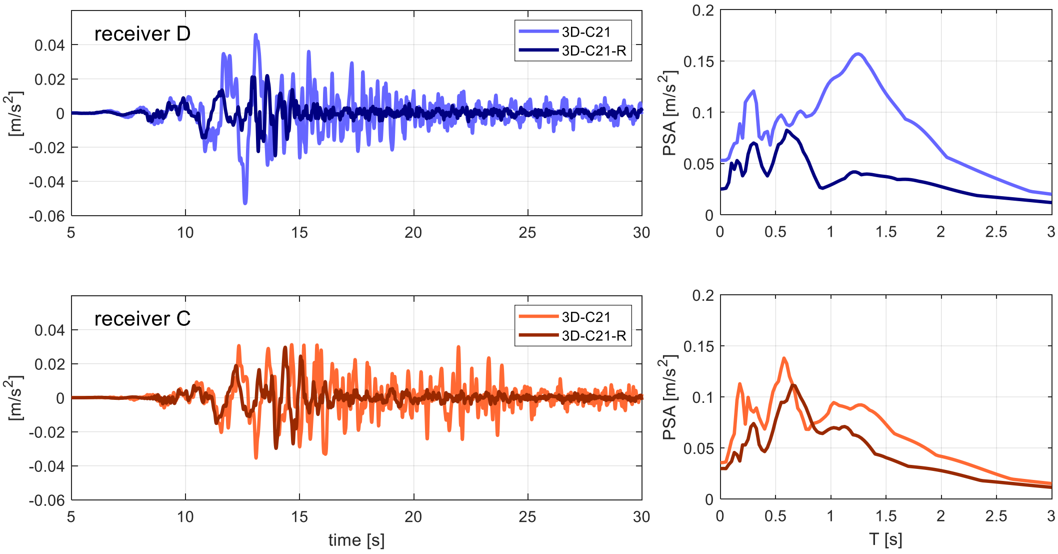

Figure 16. Comparison of EW acceleration time histories with and without basin (3D-C21 and 3D-C21-R simulations respectively) and corresponding acceleration response spectra (PSA), for the D (top, blue lines) and C (bottom, red lines) receivers of Figure 15. Basin thickness ranges from 250 m (receiver C) to 700 m (receiver D) while V_{S30}=500 m/s at both sites.

The quantification of site effects is further explored in Figure 17, where the Fourier Spectral Ratios (FSR) and Response Spectral Ratios (RSR) are considered, with reference to the receivers C and D: (a) label "3D" refers to the spectral ratios obtained by dividing the results of the simulation 3D-C21 over the 3D-C21-R; (b) label "1D" refers to the 1D theoretical amplification function with the local stratigraphy below the corresponding receiver; for the RSR, the accelerograms at C and D were computed by 1D convolution using as input motions the corresponding accelerograms computed in the without basin case (3D-C21-R); (c) labels

"C/B" and "C/F" (and similarly for receiver D) refer to the spectral ratios computed from 3D-C21 run with respect to reference stations B and F, located on the left and right side of the basin respectively (see Figure 15).

Several remarks can be made based on the inspection of Figure 17:

- with some exceptions in relatively small frequency intervals, the FSR show that there is an overall good agreement between the 1D and 3D amplification functions, supporting the accuracy of the numerical results in a relatively broad frequency range;

- in agreement with studies aiming at quantifying the aggravation factors on the response spectra related to complex 2D/3D geological configurations (e.g., Chávez-García and Faccioli, 2000; Riga et al., 2016), the 1D solution tends to overestimate the 3D one close to the basin edge (receiver C), while the opposite occurs at the basin centre (receiver D). However, comparison of RSR at short periods suggests that PGA from 3D simulations tends to be smaller than in the 1D case;

- if site amplification functions are computed with respect to a reference station, the location of such station with respect to the basin is critical (as also shown in Smerzini et al. 2011): namely, spectral ratios with respect to receiver F show some sharp anomalies, since F lies on the other side of the Rhône basin with respect to the source, so that a part of the frequency content, including low and high frequencies, is filtered out by the presence of the basin; spectral ratios with respect to receiver B are instead closer to the 1D and 3D solutions.

More generally these results confirm that, when complex geological configurations lie in the vicinity of active faults, the main features of seismic response cannot be reliably captured by standard approaches owing to the variability of the source-to-site ray paths affecting wave propagation. In these conditions, especially in case of critical structures such as NPPs, PBS seem to be an effective way to predict the regional as well as the site-specific features of the seismic response.

Further investigations are planned, starting from this case study, aiming at evaluating the variability of site effects from different realization of earthquakes from the same source, with variable magnitude and slip distribution, and from other sources in the investigated area, with different distance and azimuth from the site.

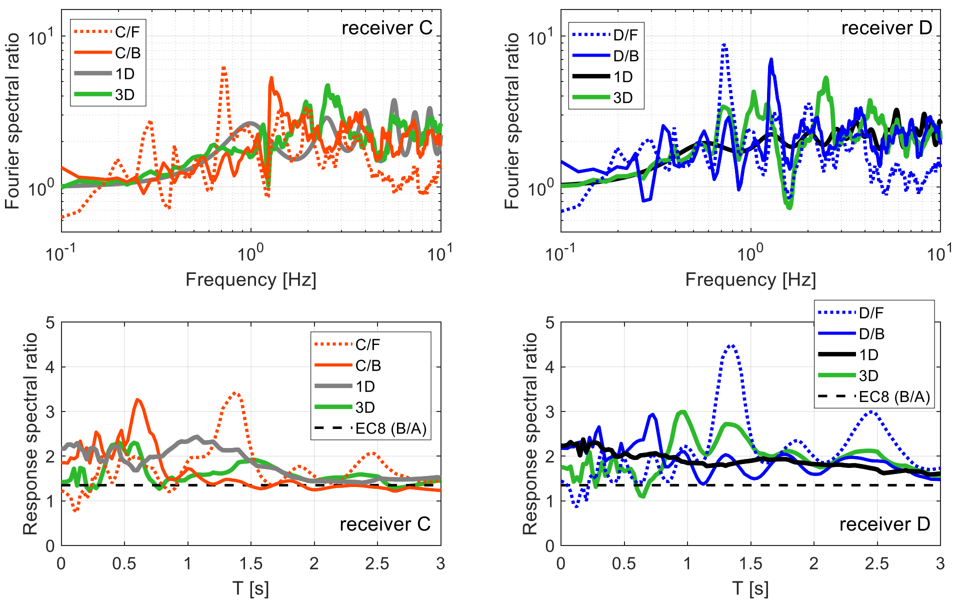

Figure 17. Comparison of amplification functions computed from Fourier spectral ratios (top) and Response spectral ratios (bottom) at the selected receivers C (left) and D (right). The plots show the spectral ratios from 3D-C21 simulations considering B and F as the reference stations on outcropping bedrock (see Figure 14 for their location). 1D refers to the local 1D theoretical amplification functions, while 3D are the spectral ratios obtained by dividing the results of the 3D-C21 run (with basin) to the 3D-C21-R one (without basin). For the response spectral ratios, the accelerograms at C and D were computed by 1D convolution using as input motions the corresponding accelerograms computed in the without basin simulation.

7 Conclusions

In this paper, a comprehensive validation exercise of physics-based numerical simulations (PBS) of seismic wave propagation is presented. The target area is an industrial region in South-Eastern France within the Rhône Valley, which hosts several operating nuclear power plants (Cruas and Tricastin). This low-to-moderate seismicity area was hit by an unusually shallow (1 km depth) Mw 4.9 earthquake rupturing the La Rouvière fault, near Le Teil, at about 15 km distance from the Cruas NPP. The recordings available for the Le Teil earthquake, although limited in number, were used for validation of the PBS. The numerical code SPEED was used for this purpose. In the recent past, this numerical code underwent several successful validations with earthquakes in a wide range of magnitudes, spanning from 3 to 6.5, and in different countries worldwide.

A model of the Earth's crust was constructed, including the La Rouvière fault and the lower Rhône Valley, with a size of 70 km × 45 km × 8.5 km and a total of about 82 millions nodes using a spectral degree SD=4. Considering models with different SDs, it was found that convergence of numerical solutions was achieved up to 5 Hz within the sedimentary basin, and up to 7.5 Hz in the outcropping rock region. Since the effects of numerical dispersion were found to be small in a broad frequency range, the numerical solutions were eventually filtered below 10 Hz and no hybrid technique was applied to produce broadband signals.

When comparing simulations with records, a good to excellent agreement was found for all explored frequency ranges, showing that, even without a very detailed 3D velocity model, the 3D PBS may provide realistic broadband predictions of earthquake ground motion. This also demonstrates that, with limited recordings available (as for the low-to-moderate seismicity region of Montélimar), PBS, if suitably calibrated and validated, can be employed to shed light on a variety of aspects related to ground motion modelling, poorly addressed by classic ergodic empirical ground motion models, spanning from the prediction of ground shaking intensity and spatial variability in the proximity of the seismic source, to region- and site- specific features of ground response. The investigation of such aspects is particularly relevant when performing seismic risk evaluation of critical infrastructures, such as e.g. NPPs. For such facilities the definition of the seismic hazard at long return periods may take advantage of both empirical and physics-based numerical approaches for ground motion characterization.

In addition to these advantages, PBS may provide a kind of numerical laboratory, where realistic time histories of ground motion can be obtained, under fully controlled knowledge of the dynamic parameters affecting the seismic wave propagation and of the slip distribution along the fault. Moreover, PBS may provide a wealth of information on key issues related to earthquake ground motion, such as explored in this paper with the investigation on the basin-induced site amplification within the Rhône Valley, that was shown to provide physically sound results in a broad frequency range.

Acknowledgements

This work was supported by swissnuclear as part of the research activity "Development of advanced numerical approaches for earthquake ground motion prediction," developed in the framework of the SIGMA-2 project. The authors acknowledge the contribution given by Ilario Mazzieri in deriving the 3D basin shape model.

References

AFPS (2021) Séisme du 11 novembre 2019 – Retour d'expérience de la gestion de crise communale. AFPS and Le Teil Municipality joint report, juin 2021, 52 pp, in French.

Ameri G, Hollender F, Perron V, Martin C (2017) Site-specific partially nonergodic PSHA for a hard-rock critical site in southern France: adjustment of ground motion prediction equations and sensitivity analysis. Bull Earthquake Eng., 15: 4089–4111.

Anderson JG (2004) Quantitative measure of the goodness-of-fit of synthetic seismograms. 13th World Conf. on Earthquake Engineering, Vancouver, B.C., Canada, August 1-6, Paper No. 243

Biro Y, Renault P (2012) Importance and Impact of Host-to-Target Conversions for Ground Motion Prediction Equations in PSHA, Proc. 15th World Conf. in Earthq. Eng., Lisbon, Portugal.

Boore DM (2010). Orientation-Independent, Nongeometric-Mean Measures of Seismic Intensity from Two Horizontal Components of Motion. Bull Seism Soc Am, 100(4), 1830–1835, August, doi: 10.1785/0120090400

Cara M, Cansi Y, Schlupp A, Arroucau P, Béthoux N, Beucler E ... & Van Der Woerd K (2015). SI-Hex: a new catalogue of instrumental seismicity for metropolitan France. Bulletin de la Société Géologique de France, 186(1), 3-19.

Causse M, Cornou C, Maufroy E et al. (2021) Exceptional ground motion during the shallow Mw 4.9 2019 Le Teil earthquake, France. Commun Earth Environ 2, 14. https://doi.org/10.1038/s43247-020-00089-0

Chávez-García FJ, Faccioli E (2000) Complex site effects and building codes: making the leap. J Seismol, 4: 23-40

Cornou C, Ampuero JP, Aubert C, Audin L, Baize S, Billant J, et al. (2021) Rapid response to the Mw 4.9 earthquake of November 11, 2019 in Le Teil, Lower Rhône Valley, France. Comptes Rendus. Géoscience, Académie des sciences (Paris), 2021, 353 (S1), pp.1-23. ff10.5802/crgeos.30ff. ffhal-03089600v2ff DOI: 10.5802/crgeos.30

Crempien JGF, Archuleta RJ. (2015). UCSB method for simulation of broadband ground motion from kinematic earthquake sources. Seismol Res Lett. 86:61. https://doi.org/10.1785/0220140103

Delouis B, Ampuero JP, Aundin L, et al. (2019). Rapport d'évaluation du groupe de travail (GT) CNRS-INSU sur le séisme du Teil du 11 novembre 2019 et ses causes possibles. 35 p., in french.

De Novellis V, Convertito V, Valkaniotis S et al. (2020) Coincident locations of rupture nucleation during the 2019 Le Teil earthquake, France and maximum stress change from local cement quarrying. Commun Earth Environ 1, 20. https://doi.org/10.1038/s43247-020-00021-6

Elmi S, Busnardo R, Clavel B, Camus G, Kieffer G, Bérard P and Michaël YB (1996) Notice explicative, Carte géol. France (1/50000), feuille Aubenas (865). Orléans: BRGM, 170 p. Carte géologique par Y. Kerrien (coord.), S. Elmi, R. Busnardo, G. Camus, G. Kieffer, J. Moinereau, A.Weisbrod (1989).

Evangelista L, del Gaudio S, Smerzini C, D'Onofrio A, Festa G, Iervolino I, Landolfi L, Paolucci R, Santo A, Silvestri F (2017) Physics-based seismic input for engineering applications: a case study in the Aterno river valley, Central Italy, Bull. Earthquake Eng. 15: 2645–2671.

Faccioli E, Maggio F, Paolucci R, Quarteroni A (1997) 2D and 3D elastic wave propagation by a pseudo-spectral domain decomposition method. Journal of Seismology, 1, 237–251

Grünthal G (ed.), Musson RMW, Schwarz J, Stucchi M (1998) European Macroseismic Scale. Cahiers du Centre Européen de Géodynamique et de Séismologie, Vol. 15 - European Macroseismic Scale 1998. European Centre for Geodynamics and Seismology, Luxembourg.

El Haber E., Smerzini C., Fasan M., Saint Mard L., Vanini M., Traversa P., Paolucci R., Ameri G. and Renault P. (2022) Simulation Techniques benchmark, the test case of the November 11, 2019 Mw4.9 Le Teil earthquake. Deliverable SIGMA2-2021-D3-082 2022.

Hisada Y, Bielak J. (2003). A theoretical method for computing near-fault ground motions in layered half-spaces considering static offset due to surface faulting, with a physical interpretation of fling step and rupture directivity. Bull Seismol Soc Am.;93(3):1154-1168.

IAEA, INTERNATIONAL ATOMIC ENERGY AGENCY (2022) Seismic Hazards in Site Evaluation for Nuclear Installations, Specific Safety Guides, SSG-9, Rev 1.

Infantino M, Mazzieri I, Ozcebe AG, Paolucci R, Stupazzini M (2020) 3D Physics-Based Numerical Simulations of Ground Motion in Istanbul from Earthquakes along the Marmara Segment of the North Anatolian Fault, Bull. Seism. Soc. Am. 110: 2559–2576.

Jomard H. et al. (2017). Transposing an active fault database into a seismic hazard fault model for nuclear facilities—Part 1: Building a database of potentially active faults (BDFA) for metropolitan France. Nat. Hazards Earth Syst. Sci. 17, 1573–1584

Kotha SR, Weatherill G, Bindi D, Cotton F (2020). A regionally-adaptable ground-motion model for shallow crustal earthquakes in Europe, Bulletin of Earthquake Engineering, 18: 4091 – 4125. https://doi.org/10.1007/s10518-020-00869-1

Landwehr N, Kuehn NM, Scheffer T, Abrahamson N (2016). A nonergodic ground-motion model for California with spatially varying coefficients, Bull. Seismol. Soc. Am. 106, no. 6, 2574–2583, doi: 10.1785/0120160118.

Mazzieri I, Stupazzini M, Guidotti R, Smerzini C (2013) SPEED: SPectral Elements in Elastodynamics with Discontinuous Galerkin: A non-conforming approach for 3D multi-scale problems, Int. J. Numer. Meth. Eng. 95, no. 12, 991–1010.

McCallen D, Petersson A, Rodgers A, Pitarka A, Miah M, Petrone F, Sjogreen B, Abrahamson N, Tang H (2021) EQSIM—A multidisciplinary framework for fault-to-structure earthquake simulations on exascale computers part I: Computational models and workflow, Earthquake Spectra, 37(2), 707–735.

Mordret A, Brenguier F, Causse M, Boué P, Voisin C, Dumont I, Vernon FL, Ampuero JP (2020). Seismic stereometry reveals preparatory behavior and source kinematics of intermediatesize earthquakes. Geophysical Research Letters, 47, e2020GL088563. https://doi.org/10.1029/2020GL088563 .

Paolucci R, Mazzieri I, Smerzini C (2015). Anatomy of strong ground motion: Near-source records and three-dimensional physics-based numerical simulations of the Mw 6.0 2012 May 29 Po Plain earthquake, Italy, Geophysical Journal International, 203(3): 2001–2020.

Paolucci R, Infantino M, Mazzieri I, Özcebe AG, Smerzini C, Stupazzini M (2018) 3D physics-based numerical simulations: advantages and current limitations of a new frontier to earthquake ground motion prediction. In Recent Advances in Earthquake Engineering in Europe (K. Pitilakis ed.), Geotechnical, Geological and Earthquake Engineering series, Vol. 46, Chapter 8, 203-223, Springer.

Paolucci R, Mazzieri I, Piunno G, Smerzini C, Vanini M, Özcebe AG (2021). Earthquake ground motion modelling of induced seismicity in the Groningen gas field, Earthq. Eng. Struct. Dynam. 50, 135–154, doi: 10.1002/eqe.3367

Ramadan F, Smerzini C, Lanzano G, Pacor F (2021) An empirical model for the vertical-to-horizontal spectral ratios for Italy. Earthquake Engineering and Structural Dynamics 50(15): 3937-4219.

Ramadan F, Lanzano G, Smerzini C, Pacor F, Traversa P, Felicetta Chiara (2022) Prediction Models for Vertical Ground Motion for Italy and France, 3rd European Conference on Earthquake Engineering and Seismology, Bucharest, Romania.

Regnier J, Laurendeau A, Duvel AM, Guéguen P (2010) From heterogeneous set of soil data to Vs profile: application to the French accelerometric network (RAP) sites. 14th European Conference on Earthquake Engineering.

Riga E, Makra K, Pitilakis K (2016). Aggravation factors for seismic response of sedimentary basins: A code-oriented parametric study, Soil Dynamics and Earthquake Engineering 91, 116–132.

Ritz JF, Baize S, Ferry M et al. (2020). Surface rupture and shallow fault reactivation during the 2019 Mw 4.9 Le Teil earthquake, France. Commun Earth Environ 1, 10. https://doi.org/10.1038/s43247-020-0012-z

Sangaraju S, Paolucci R, Smerzini C (2021). 3D physics-base ground motion simulation of the 2016 Kumamoto earthquakes. 6th IASPEI / IAEE International Symposium: Effects of Surface Geology on Seismic Motion, August.

Schlupp A, Sira C, Maufroy E, Provost L, Dretzen r, Bertrand E, Beck E, Schaming M (2021). EMS98 intensities distribution of the “Le Teil” earthquake, France, 11 November 2019 (Mw 4.9) based on macroseismic surveys and field investigations. Comptes Rendus. Géoscience, Volume 353 no. S1, pp. 465-492. doi 10.5802/crgeos.88. https://comptes-rendus.academie-sciences.fr/geoscience/articles/10.5802/crgeos.88/

Sira C, Schlupp A, Maufroy E, Provost L, Dretzen R, Bertrand E, Beck E, Schaming M. (2020). Rapport macrosismique n– 4, Séisme du Teil (Ardèche) 11 novembre 2019 à 11 h 52 locale, Magnitude 5,2 ML (RENASS), Intensité communale max VII–VIII (EMS98, BCSF-Rénass-2020-R2).

Smerzini C, Paolucci R, Stupazzini M (2011). Comparison of 3D, 2D and 1D numerical approaches to predict long period earthquake ground motion in the Gubbio plain, Central Italy, Bull. Earthq. Eng. 9, no. 6, 2007–2029.

Stafford PJ, Rodriguez-Marek A, Edwards B, Kruiver PP, Bommer JJ (2017) Scenario Dependence of Linear Site-Effect Factors for Short-Period Response Spectral Ordinates. Bull Seism Soc Am 107(6): 2859–2872.

Stewart JP, Boore DM, Seyhan E, Atkinson GM (2016). NGA-West2 Equations for Predicting Vertical-Component PGA, PGV, and 5%-Damped PSA from Shallow Crustal Earthquakes Earthquake Spectra, Volume 32, No. 2, pages 1005–1031, May 2016; © 2016, Earthquake Engineering Research Institute.

Stupazzini M, Paolucci R, Igel H (2009) Near-Fault Earthquake Ground-Motion Simulation in the Grenoble Valley by a High-Performance Spectral Element Code," Bull. Seismol. Soc. Am., 99(1): 286–301.

Sung C H, Abrahamson N, Kuehn NM, Traversa P, Zentner I (2022). A Non-Ergodic Ground-Motion Model of Fourier Amplitude Spectra for France. Accepted for publication, DOI: 10.21203/rs.3.rs-358937/v1

Funding

The work has been funded by swissnuclear within the 2017-2022 research project "Development of advanced numerical approaches for earthquake ground motion prediction".

Competing interests

The authors declare that they have no competing financial interests or personal relationships that could have appeared to influence the work reported in this paper.

Data Availability

The SPEED code is available at http://speed.mox.polimi.it. The simulations and data generated during the current study are available from the corresponding author on reasonable request.